MOX-Report No. 55/2018

Mathematical analysis, finite element approximation and numerical solvers for the interaction of 3D reservoirs with 1D wells

Cerroni, D.; Laurino, F.; Zunino, P.

MOX, Dipartimento di Matematica
Politecnico di Milano, Via Bonardi 9 - 20133 Milano (Italy)

mox-dmat@polimi.it http://mox.polimi.it

Springer Journals manuscript No.
(will be inserted by the editor)

Mathematical analysis, finite element approximation and numerical solvers for the interaction of 3D reservoirs with 1D wells

Daniele Cerroni · Federica Laurino · Paolo Zunino

Received: date / Accepted: date

Abstract We develop a mathematical model for the interaction of a three-dimensional reservoir with the flow through wells, namely narrow cylindrical channels cutting across the reservoir. Leak off or sink effects are taken into account. To enable the simulation of complex configurations featuring multiple wells, we apply a model reduction technique that represents the wells as one-dimensional channels. The challenge in this case is to account for the interaction of the reservoir with the embedded one-dimensional wells. The resulting problem consists of coupled partial differential equations defined on manifolds with heterogeneous dimensionality. The existence and regularity of weak solutions of such problem is thoroughly addressed. Afterwards, we focus on the numerical discretization of the problem in the framework of the finite element method. We notice that the numerical scheme does not require conformity between the computational mesh of the reservoir and the one of the wells. From the standpoint of the solvers, we discuss the application of multilevel algorithms, such as the algebraic multigrid method. Finally, the reduced mathematical model and the discretization method is applied to a few configurations of reservoir with wells, with the purpose of verifying the theoretical properties and to assess the generality of the approach.

Keywords perforated reservoirs · dimensional model reduction · finite elements · multigrid solvers

1 Introduction

The simulation of multiscale, multiphysics, multimodel systems is among the grand challenges in Computational Science & Engineering. In this context, the application of topological (or geometrical) model reduction techniques plays an essential role. For example, small inclusions of a continuum can be described as zero-dimensional (0D) or one-dimensional (1D) concentrated sources in order to reduce the computational cost of simulations. Many problems in this area are not well investigated yet, such as the coupling of three-dimensional (3D) continua with embedded (1D) networks, although it arises in applications of paramount importance such as flow through perforated media.

Despite the literature of computational models for describing fractured reservoirs is extremely rich and lively (it would be excessively reductive to make some examples here) the analogous problem of the interaction of reservoirs with wells is much less explored. Indeed, the seminal work by D.W. Peaceman

Daniele Cerroni
MOX, Department of Mathematics, Politecnico di Milano
E-mail: daniele.cerroni@polimi.it

Federica Laurino
MOX, Department of Mathematics, Politecnico di Milano
Istituto Italiano di Tecnologia, Genova, Italy
E-mail: federica.laurino@polimi.it

Paolo Zunino
MOX, Department of Mathematics, Politecnico di Milano
E-mail: paolo.zunino@polimi.it

[21,23,22] is still widely used by the scientific community. Only recently (with respect to the previous works) some new approaches have been proposed [1,5,11,28,29].

Our objective is contributing to the development of advanced computational models for the interaction of reservoirs with wells. We aim to develop an approach that is appealing for industrial applications, involving realistic geological models and real configurations of multiple wells. A simplified sketch of the applications we aim to address is reported in Figure 1. For this reason, we adopt a geometrical model reduction technique that transforms the flow equations in the wells into a 1D model. The resulting problem consists of coupled partial differential equations (PDEs) on manifolds with heterogeneous dimensionality. This approach was originally proposed in [6,7,8]. It has recently attracted the attention of several researchers from the perspective of theory and applications. On one hand, it requires particular attention to prove existence of a solution in the weak (or variational) sense [13,14,12,15,2,19]. On the other hand, it is relevant for applications to microcirculation [3,4,17,18].

After discussing the model, we discretize the equations using the finite element method (FEM) and we focus on the computational aspects of the problem. Even though FEM is a well established computational method and several open-source and commercial numerical solvers are available, the implementation of general three-dimensional FEM solvers able to efficiently handle one or two-dimensional inclusions is still a significant challenge for the scientific computing community.

The method proposed here facilitates this task, because it does not require conformity between the computational mesh of the reservoir and the one of the wells. However, because of the non-standard coupling of the flow problems in 3D and 1D, the algebraic structure of the discrete problem is modified with respect to the standard FEM case. For this reason, with a few test cases with increasing complexity, we present and discuss preliminary results on the application of high performance, multilevel algebraic solvers to this problem.

This work is organized as follows. In Section 2, we address the full model formulation and we thoroughly describe the topological model reduction technique. We also derive the variational formulation of the reduced problem. Then, in Section 3 we study the well posedness and the regularity of the weak problem, which can be cast in the framework of the Lax-Milgram lemma. The numerical discretization is performed and analyzed in Section 4, with particular attention to the application of multigrid solvers. Finally, in Section 5 we discuss the numerical results in view of the available theory and we apply the computational model to some simplified configurations of 1D wells embedded into 3D reservoirs.

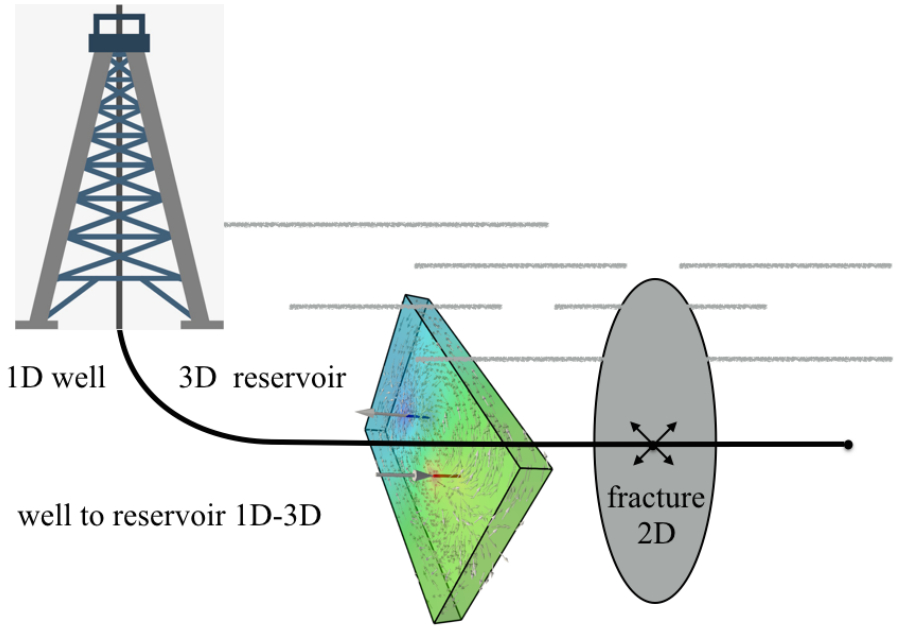

Fig. 1: A sketch of the problem involving the interaction of a reservoir with wells.

2 Problem setting for a reservoir with one well

The domain is denoted as Ω and composed by two parts, Ω_w and $\Omega_p = \Omega \setminus \overline{\Omega}_w$, where $\overline{\Omega}_w$ denotes the closure of Ω_w. We assume that Ω_w is the well and Ω_p the surrounding reservoir. Let Ω_w be a cylinder swept by a circle of radius ρ along a curve. More precisely, let $\boldsymbol{\lambda}(s) = [\xi(s), \nu(s), \zeta(s)],\ s \in (0, S)$ be a $\mathcal{C}^2$-regular curve in the three-dimensional space. Let $\Lambda = \{\boldsymbol{\lambda}(s),\ s \in (0, S)\}$ be the centerline of the cylinder. For simplicity, let us assume that $\|\boldsymbol{\lambda}'(s)\| = 1$ such that the arc-length and the coordinate s coincide. Let $\boldsymbol{T}, \boldsymbol{N}, \boldsymbol{B}$ be the Frenet frame related to the curve. Let $\mathcal{D} = [r\cos\theta, r\sin\theta] : [0, \rho) \times [0, 2\pi) \to \boldsymbol{R}^2$ be a parametrization of the cross section. Let us also define the boundary of the cross section as $\partial\mathcal{D} = [\rho\sin\theta, \rho\cos\theta] : [0, 2\pi) \to \boldsymbol{R}^2$. Then, the cylinder Ω_w can be defined as follows

$$\Omega_w = \{\boldsymbol{\lambda}(s) + r\cos\theta\boldsymbol{N}(s) + r\sin\theta\boldsymbol{B}(s),\ r \in [0, \rho),\ s \in (0, S),\ \theta \in [0, 2\pi)\}\,,$$

and the lateral boundary of it, denoted with Γ is,

$$\Gamma = \{\boldsymbol{\lambda}(s) + \rho\cos\theta\boldsymbol{N}(s) + \rho\sin\theta\boldsymbol{B}(s),\ s \in (0, S),\ \theta \in [0, 2\pi)\}\,.$$

We notice that Ω_w has *top* and *bottom* boundaries, which are $\partial\Omega_w \setminus \Gamma = \{\boldsymbol{\lambda}(0) + \mathcal{D}\} \cup \{\boldsymbol{\lambda}(S) + \mathcal{D}\}$. To model wells, without loss of generality, we assume that $\{\boldsymbol{\lambda}(0) + \mathcal{D}\}$ is the injection section of the well and for this reason it belongs to the external boundary, namely $\partial\Omega_p$. The other well tip, $\{\boldsymbol{\lambda}(S) + \mathcal{D}\}$ may be embedded into the reservoir.

Let $\boldsymbol{u}_p, p_p$ be the velocity and pressure in the reservoir Ω_p. We assume that the reservoir is described as a porous medium. By consequence, average velocity and pressure on a representative volume obey to Darcy's law. Let $\boldsymbol{u}_w, p_w$ be the velocity and pressure of fluid injected or extracted through the well. We model the well by means of pressure-driven flow. More precisely, we assume that the pressure gradient is the main driving force for the flow motion. This is a fairly general assumption that can be motivated in different ways. On one hand, it is verified by the Poiseuille flow, that can be seen as a particular case of Stokes-like flow applied to straight cylinders. On the other hand, it would also be true for a Darcy-type flow, where the motion is determined by the interaction between pressure and friction. For the sake of simplicity (homogeneity with the reservoir model) we adopt the second standpoint, but we remark that the mathematical structure of the final governing equations would be the same in the former case. However, the coefficients of the equations would differ in the two cases. Let $\boldsymbol{K}_p$ and $\boldsymbol{K}_w$ be the permeability tensors in the reservoir and in the well, respectively. We assume that these are symmetric positive definite tensors and that there exist constants K_p, $K_w > 0$ such that $\boldsymbol{v}^T\boldsymbol{K}_*\boldsymbol{v} \geq K_*\|\boldsymbol{v}\|^2$ with $* = p, w$. Finally, it is assumed that the interface Γ is permeable, namely it is crossed by a normal flux proportional to $K_\Gamma\,(p_p - p_w)$. The coefficient $K_\Gamma \geq 0$ denotes the permeability of the borehole lateral surface. It can take null values on part of the well.

For the boundary conditions, without loss of generality, we have prescribed that the pressure is fixed to values $p_{w,0}$, $p_{w,1}$ at the endpoints of the well. For the reservoir, we split $\partial\Omega_p \setminus \Gamma$ into two complementary parts, namely Σ_N, Σ_D such that $\Sigma_N \cup \Sigma_D = \partial\Omega_p \setminus \Gamma$. On Σ_N we set Robin-type boundary conditions, where the parameter $K_{\partial\Omega}$ may also vanish and $p_{p,0}$ stands for a reference pressure outside the reservoir, e.g. the hydrostatic pressure. On Σ_D we set Dirichlet type condition, for a given pressure value $p_{p,1}$.

As a result of these assumptions, we describe flow and pressure in the system by means of the following prototype problem,

$$\begin{cases} \nabla\cdot\boldsymbol{u}_p = 0, \quad \boldsymbol{u}_p + \boldsymbol{K}_p\nabla p_p = 0 & \text{in } \Omega_p, \\ \nabla\cdot\boldsymbol{u}_w = 0, \quad \boldsymbol{u}_w + \boldsymbol{K}_w\nabla p_w = 0 & \text{in } \Omega_w, \\ \boldsymbol{u}_p\cdot\boldsymbol{n}_p = K_\Gamma\,(p_p - p_w) & \text{on } \Gamma, \\ \boldsymbol{u}_w\cdot\boldsymbol{n}_w = K_\Gamma\,(p_w - p_p) & \text{on } \Gamma, \\ \boldsymbol{u}_p\cdot\boldsymbol{n}_p = K_{\partial\Omega}\,(p_p - p_{p,0}) & \text{on } \Sigma_N, \\ p_p = p_{p,1} & \text{on } \Sigma_D, \\ p_w = p_{w,0} & \text{on } \{\boldsymbol{\lambda}(0) + \mathcal{D}\}, \\ p_w = p_{w,1} & \text{on } \{\boldsymbol{\lambda}(S) + \mathcal{D}\}\,. \end{cases} \tag{1}$$

2.1 Topological model reduction & coupled problems with hybrid dimensionality

The objective of this work is to consider a simplified version of problem (1), where the domain Ω_w shrinks to its centerline Λ and the corresponding partial differential equation is averaged on the cylinder cross section $\mathcal{D}$. This new problem setting will be also called the *reduced problem*. Form the mathematical standpoint it is more challenging than (1), because it involves the coupling of 3D/1D elliptic equations.

Before proceeding, let us reformulate (1) as a problem for the pressure variables solely. We obtain the following equations,

$$\begin{cases} -\nabla \cdot (\boldsymbol{K}_p \nabla p_p) = 0 & \text{in } \Omega_p, \\ -\nabla \cdot (\boldsymbol{K}_w \nabla p_w) = 0 & \text{in } \Omega_w, \\ -\boldsymbol{K}_p \nabla p_p \cdot \boldsymbol{n}_p = K_\Gamma \left(p_p - p_w\right) & \text{on } \Gamma, \\ -\boldsymbol{K}_w \nabla p_w \cdot \boldsymbol{n}_w = K_\Gamma \left(p_w - p_p\right) & \text{on } \Gamma, \\ -\boldsymbol{K}_p \nabla p_p \cdot \boldsymbol{n}_p = K_{\partial\Omega} \left(p_p - p_{p,0}\right) & \text{on } \Sigma_N, \\ p_p = p_{p,1} & \text{on } \Sigma_D, \\ p_w = p_{w,0} & \text{on } \{\boldsymbol{\lambda}(0) + \mathcal{D}\}, \\ p_w = p_{w,1} & \text{on } \{\boldsymbol{\lambda}(S) + \mathcal{D}\}. \end{cases} \tag{2}$$

Then, let us scale the domains Ω_p and Ω_w and let us rewrite the equations in dimensionless form. More precisely, let $\chi_{\Omega_p}(\boldsymbol{x}) = \boldsymbol{x}/L$ where $L = \text{diam}(\Omega_p)$ be a scaling function and let be $\Omega_{p_\chi} = \chi_{\Omega_p}(\Omega_p)$, $\Omega_{w_\chi} = \chi_{\Omega_p}(\Omega_w)$ be the scaled domains. For simplicity of notation, and without loss of generality, form now on we will implicitly refer to the scaled domains dropping the sub-index χ. For the derivation of the dimensionless form of the equations, we take L as the characteristic length, $p_{w,0}$ as the characteristic pressure and K_p as the reference permeability. The dimensionless pressure is denoted as $u_* = p_*/p_{w,0}$, which represents the unknown of the dimensionless problem. Then, problem (2) is equivalent to find u_p, u_w such that,

$$\begin{cases} -\nabla \cdot (\boldsymbol{k}_p \nabla u_p) = 0 & \text{in } \Omega_p, \\ -\nabla \cdot (\boldsymbol{k}_w \nabla u_w) = 0 & \text{in } \Omega_w, \\ -\boldsymbol{k}_p \nabla u_p \cdot \boldsymbol{n}_p = \kappa \left(u_p - u_w\right) & \text{on } \Gamma, \\ -\boldsymbol{k}_w \nabla u_w \cdot \boldsymbol{n}_w = \kappa \left(u_w - u_p\right) & \text{on } \Gamma, \\ -\boldsymbol{k}_p \nabla u_p \cdot \boldsymbol{n}_p = \mu \left(u_p - \frac{p_{p,0}}{p_{w,0}}\right) & \text{on } \Sigma_N, \\ u_p = \frac{p_{p,1}}{p_{w,0}} & \text{on } \Sigma_D, \\ u_w = 1 & \text{on } \{\boldsymbol{\lambda}(0) + \mathcal{D}\}, \\ u_w = \frac{p_{w,1}}{p_{w,0}} & \text{on } \{\boldsymbol{\lambda}(S) + \mathcal{D}\}. \end{cases} \tag{3}$$

where we have denoted with $\boldsymbol{k}_* = \boldsymbol{K}_*/K_p$ the dimensionless permeability tensors, $\kappa = (K_\Gamma L)/K_p$ is the dimensionless permeability of the borehole lateral surface and $\mu = (K_{\partial\Omega} L)/K_p$ is the permeability at the external surface of the reservoir. For notational convenience, but without loss of generality, from now on we will assume that the external pressures $p_{p,0}$, $p_{p,1}$, $p_{w,1} = 0$. In this way, all the external forcing terms of the problem vanish, except from the unit injection pressure.

2.1.1 Topological model reduction of the well

The disadvantage of modelling a narrow borehole in three dimensions is that it requires the resolution of the geometry, which in many real applications can be difficult to handle in the context of a reservoir model. Therefore we apply a topological model reduction, namely we go from a 3D-3D to a 3D-1D formulation. The model reduction approach that we adopt is based on the following fundamental assumption:

A0) *The diameter of the well is small compared to the diameter of the reservoir.*

The previous assumption implies that for the scaled domains the radius of the borehole $R = \rho/L$ is such that $0 < R \ll 1$. As a consequence of the previous fundamental assumption we formulate also the following:

A1) the function u_w has a *uniform profile* on each cross section $\mathcal{D}$, namely in cylindrical coordinates $u_w(r,s,\theta) = U(s)$. We make a similar assumption on the coefficients of the problem. The permeability tensor in the borehole is isotropic, namely $\boldsymbol{k}_w = k_w \boldsymbol{I}$ and it is uniform on each cross section of the hole, that is $k_w(r,s,\theta) = k_w(s)$. The same restriction is enforced on the parameter κ on Γ, precisely $\kappa(\theta,s) = \kappa(s)$.

Since the derivation of the reduced model is based on averaging, we introduce the following notation,

$$\int_\Lambda \int_{\mathcal{D}} w d\sigma ds = \int_\Lambda \pi R^2 \overline{\overline{w}}(s) ds\,,$$
$$\int_\Lambda \int_{\partial\mathcal{D}} w d\gamma ds = \int_\Lambda 2\pi R \overline{w}(s) ds\,,$$

where $\overline{\overline{w}}$, $\overline{w}$ denote the following mean values respectively,

$$\overline{\overline{w}}(s) = (\pi R^2)^{-1} \int_{\mathcal{D}} w d\sigma\,,$$
$$\overline{w}(s) = (2\pi R)^{-1} \int_{\partial\mathcal{D}} w d\gamma\,,$$

and $d\omega = r\, d\theta\, dr\, ds$, $d\sigma = r\, d\theta\, dr$, $d\gamma = R\, d\theta$ represent volume, surface and curvilinear measures.

We apply the averaging technique to equation (3). In particular, we consider an arbitrary portion $\mathcal{P}$ of the cylinder, bounded by two perpendicular sections to Λ with $s_1 < s_2$. We have,

$$\int_{\mathcal{P}} \nabla\cdot(k_w \nabla u_w) d\Omega = \int_{\partial\mathcal{P}} k_w \nabla u_w \cdot \boldsymbol{n}_w = -\int_{\mathcal{D}(s_1)} k_w \partial_s u_w d\sigma + \int_{\mathcal{D}(s_2)} k_w \partial_s u_w d\sigma + \int_\Gamma k_w \nabla u_w \cdot \boldsymbol{n}_w d\sigma$$

By the fundamental theorem of integral calculus we have,

$$-\int_{\mathcal{D}(s_1)} k_w \partial_s u_w d\sigma + \int_{\mathcal{D}(s_2)} k_w \partial_s u_w d\sigma = \int_{s_1}^{s_2} d_s \left(\int_{\mathcal{D}} (k_w \partial_s u_w) d\sigma \right) ds = \int_{s_1}^{s_2} \pi R^2 d_s (k_w \partial_s \overline{\overline{u}}_w) ds$$

By means of the interface conditions between the well and the reservoir we obtain,

$$\int_\Gamma -k_w \nabla u_w \cdot \boldsymbol{n}_w d\sigma = \int_\Gamma \kappa(u_w - u_p) d\sigma = \int_{s_1}^{s_2} \int_{\partial\mathcal{D}} \kappa(u_w - u_p) R d\theta ds = \int_{s_1}^{s_2} 2\pi R \kappa (\overline{u}_w - \overline{u}_p) ds\,.$$

From the combination of all the above terms with the right hand side, we obtain that the solution u_w of (3) satisfies,

$$\int_{s_1}^{s_2} \left[-\pi R^2 d_s (k_w \partial_s \overline{\overline{u}}_w) + 2\pi R \kappa (\overline{u}_w - \overline{u}_p) \right] ds = 0\,.$$

Since the choice of the points s_1, s_2 is arbitrary, we conclude that the following equation holds true,

$$-\pi R^2 d_s (k_w \partial_s \overline{\overline{u}}_w) + 2\pi R \kappa (\overline{u}_w - \overline{u}_p) = 0 \quad \text{on } \Lambda\,. \tag{4}$$

Using the boundary conditions we conclude that the function $u_w(r,s,\theta) = U(s)$ satisfies the following equations on Λ,

$$-\pi R^2 d_s (k_w d_s U) + 2\pi R \kappa U = 2\pi R \kappa \overline{u}_p \qquad \text{on } \Lambda\,, \tag{5a}$$
$$U = 1 \qquad \text{on } s = 0 \tag{5b}$$
$$U = 0 \qquad \text{on } s = S\,. \tag{5c}$$

The weak form of the previous problem consists to find $U \in H_0^1(\Lambda)$ such that

$$\pi R^2 (k_w d_s U, d_s V)_\Lambda + 2\pi R (\kappa U, V)_\Lambda = 2\pi R (\kappa(\overline{u}_p - W), V)_\Lambda, \quad \forall V \in H_0^1(\Lambda)\,, \tag{6}$$

where $W = 1 - s$ denotes a suitable linear lifting of the Dirichlet boundary conditions of U on Λ.

2.1.2 Topological model reduction of the interface conditions

Let us now consider the weak formulation of equation (3) that govern the pressure on Ω_p. Integrating by parts and using boundary and interface conditions, we obtain:

$$\begin{aligned} 0 &= \int_{\Omega_p} \nabla \cdot (-\boldsymbol{k}_p \nabla u_p) v \, d\omega = \int_{\Omega_p} \boldsymbol{k}_p \nabla u_p \cdot \nabla v \, d\omega - \int_{\partial\Omega_p} \boldsymbol{k}_p \nabla u_p \cdot \boldsymbol{n}_p v \, d\sigma = \\ &= \int_{\Omega_p} \boldsymbol{k}_p \nabla u_p \cdot \nabla v \, d\omega + \int_{\Sigma_N} \mu u_p v \, d\sigma + \int_{\Gamma} \kappa u_p v \, d\sigma - \int_{\Gamma} \kappa u_w v \, d\sigma, \ \forall v \in H^1_{\Sigma_D}(\Omega). \end{aligned} \tag{7}$$

Let us split the solutions and the test functions on Γ, namely $u_*|_\Gamma$ for $* = p, w$ and $v|_\Gamma$, as their average plus some fluctuation, namely

$$u_* = \overline{u}_* + \tilde{u}_*, \qquad v = \overline{v} + \tilde{v},$$

where $\overline{\tilde{v}} = 0$ for any function. Therefore, using the cylindrical coordinates system (s, θ) on Γ, we have

$$\int_\Gamma \kappa u_* v \, d\sigma = \int_\Lambda \kappa(s) \int_0^{2\pi} (\overline{u}_* + \tilde{u}_*)(\overline{v} + \tilde{v}) R \, d\theta ds = \int_\Lambda 2\pi R \kappa \overline{u}_* \overline{v} \, ds + \int_\Lambda \kappa \int_0^{2\pi} \tilde{u}_* \tilde{v} R \, d\theta ds,$$

Then, we make the following modelling assumptions:

A2) we identify the domain Ω_p with the entire Ω, and we correspondingly omit the subscript p to the functions defined on Ω, namely

$$\int_{\Omega_p} v_p d\omega \simeq \int_\Omega v d\omega \,.$$

A3) we assume that the product of fluctuations is small, namely

$$\int_0^{2\pi} \tilde{u}_* \tilde{v} R \, d\theta \simeq 0 \,.$$

By means of the previous calculations, reminding that $u_w(r, s, \theta) = U(s)$, we obtain that $u \in H^1_{\Sigma_D}(\Omega)$ solves the following problem,

$$(\boldsymbol{k}_p \nabla u, \nabla v)_\Omega + (\mu u, v)_{\Sigma_N} + 2\pi R(\kappa \overline{u}, \overline{v})_\Lambda = 2\pi R(\kappa U, \overline{v})_\Lambda \,, \quad \forall v \in H^1_{\Sigma_D}(\Omega) \,, \tag{8}$$

where $H^1_{\Sigma_D}(\Omega)$ denotes the subspace of $H^1(\Omega)$ of functions with vanishing traces on Σ_D.

3 Mathematical analysis and numerical approximation of the problem

After the model reduction technique, the problem of finding the pressures u_p, u_w in the reservoir and the well, respectively, has transformed into solving a 3D problem for u in Ω and a 1D problem for U in Λ. In variational form, it consists of finding $u \in H^1_{\Sigma_D}(\Omega)$ and $U \in H^1_0(\Lambda)$ such that

$$\begin{cases} (\boldsymbol{k}_p \nabla u, \nabla v)_\Omega + (\mu u, v)_{\Sigma_N} + 2\pi R(\kappa \overline{u}, \overline{v})_\Lambda = 2\pi R(\kappa U, \overline{v})_\Lambda \,, & \forall v \in H^1_{\Sigma_D}(\Omega) \\ \pi R^2 (k_w d_s U, d_s V)_\Lambda + 2\pi R(\kappa U, V)_\Lambda = 2\pi R(\kappa(\overline{u} - W), V)_\Lambda, & \forall V \in H^1_0(\Lambda) \,. \end{cases} \tag{9}$$

For what follows, it is convenient to define the bilinear forms:

$$\begin{aligned} a_\Omega(w, v) &= (\boldsymbol{k}_p \nabla w, \nabla v)_\Omega + (\mu w, v)_{\Sigma_N} \,, \\ a_\Lambda(w, v) &= \pi R^2 (k_w d_s w, d_s v)_\Lambda \\ b_\Lambda(w, v) &= 2\pi R(\kappa w, v)_\Lambda. \end{aligned}$$

Let us now introduce a compact formulation for problem (9). In particular, we define $\mathcal{V} = [v, V]$ as a generic function of the space $\mathbb{V} = H^1_{\Sigma_D}(\Omega) \times H^1_0(\Lambda)$ and we name $\mathcal{U} = [u, U]$ the couple of unknowns of problem (9). Any function $\mathcal{V} \in \mathbb{V}$ is endowed with the norm $|||\mathcal{V}|||^2 = \|v\|^2_{H^1(\Omega)} + \|V\|^2_{H^1(\Lambda)}$. Then, we introduce the following bilinear form in $\mathbb{V} \times \mathbb{V}$,

$$\mathcal{A}(\mathcal{U}, \mathcal{V}) = a_\Omega(u, v) + a_\Lambda(U, V) + b_\Lambda(\overline{u} - U, \overline{v} - V) \,,$$

and the linear functional in $\mathbb{V}$,

$$\mathcal{F}(\mathcal{V}) = -b_\Lambda(W, V).$$

Then, the compact form of problem (9) consists of finding $\mathcal{U} \in \mathbb{V}$ such that

$$\mathcal{A}(\mathcal{U}, \mathcal{V}) = \mathcal{F}(\mathcal{V}), \quad \forall \mathcal{V} \in \mathbb{V}\,. \tag{10}$$

We name the previous problem as the *3D-1D coupled problem*. This problem is an extension to 3D of the one considered in [12]. The analysis can be pursued using the Lax-Milgram lemma. Before addressing the central result, that is Theorem 1, we present some auxiliary tools.

Lemma 1 *If $v \in H^1(\Omega)$ or alternatively $v \in L^2(\Gamma)$, then $\overline{v} \in L^2(\Lambda)$ and the following inequality holds*

$$\|\overline{v}\|^2_{L^2(\Lambda)} \leq \frac{1}{2\pi R}\|v\|^2_{L^2(\Gamma)} \leq \frac{C_T\,(\Gamma)}{2\pi R}\|v\|^2_{H^1(\Omega)}, \tag{11}$$

being $C_T\,(\Gamma)$ the (positive) constant of the trace inequality from $L^2(\Gamma)$ to $H^1(\Omega)$.

Proof Let us consider

$$\int_\Lambda \overline{v}^2\, ds = \int_\Lambda \left(\frac{1}{2\pi R}\int_0^{2\pi} vR\, d\theta\right)^2 ds = \frac{1}{4\pi^2 R^2}\int_\Lambda \left(\int_0^{2\pi} vR\, d\theta\right)^2 ds. \tag{12}$$

Using Jensen's inequality, we obtain

$$\frac{1}{4\pi^2 R^2}\int_\Lambda \left(\int_0^{2\pi} vR\, d\theta\right)^2 ds \leq \frac{1}{2\pi R}\int_\Lambda \int_0^{2\pi} v^2 R\, d\theta\, ds \tag{13}$$

and consequently

$$\int_\Lambda \overline{v}^2\, d\gamma \leq \frac{1}{2\pi R}\int_\Lambda \int_0^{2\pi} v^2 R\, d\theta\, ds = \frac{1}{2\pi R}\int_\Gamma v^2\, d\sigma = \frac{1}{2\pi R}\|v\|^2_{L^2(\Gamma)} \leq \frac{C_T\,(\Gamma)}{2\pi R}\|v\|^2_{H^1(\Omega)}. \tag{14}$$

If the inequality (11) holds, it follows immediately that $\overline{v} \in L^2(\Lambda)$, since $v \in H^1(\Omega)$.

Lemma 2 (Poincaré inequality) *For any $v \in H^1_{\Sigma_D}(\Omega)$, there exists a positive constant, $C_P(\Omega)$, s.t.*

$$\|v\|^2_{L^2(\Omega)} \leq C_P(\Omega)\|\nabla v\|^2_{L^2(\Omega)}. \tag{15}$$

We use the Poincaré inequality to control the H^1-norm of the solution by means of the energy of the problem (10). We can now address the coercivity and the continuity of the bilinear form $\mathcal{A}$.

Lemma 3 *Under the assumptions that $k_{p_{i,j}}, \in [L^\infty(\Omega)]^{3,3}$, $k_w \in L^\infty(\Lambda)$, $\kappa \in L^\infty(\Lambda)$, $\mu \in L^\infty(\Sigma_N)$, k_w is strictly positive with minimum k_{min} and κ, μ are nonnegative, the operator $\mathcal{A}$ is continuous and coercive. More precisely, there exist constants $M, m > 0$ such that,*

$$\mathcal{A}(\mathcal{U}, \mathcal{V}) \leq M|||\mathcal{U}|||\,|||\mathcal{V}|||, \quad \mathcal{A}(\mathcal{V}, \mathcal{V}) \geq m|||\mathcal{V}|||^2 \quad \forall \mathcal{U}, \mathcal{V} \in \mathbb{V}.$$

Proof The coercivity of $\mathcal{A}$ follows from (15) and the ellipticity assumption. Indeed

$$\begin{aligned} \mathcal{A}(\mathcal{V}, \mathcal{V}) &= a_\Omega(v, v) + a_\Lambda(V, V) + b_\Lambda(\overline{v} - V, \overline{v} - V) \\ &\geq a_\Omega(v, v) + a_\Lambda(V, V), \end{aligned} \tag{16}$$

being $b_\Lambda(\overline{v} - V, \overline{v} - V)$ nonnegative. For the first term, using (15) we obtain

$$\begin{aligned} a_\Omega(v, v) &= (\boldsymbol{k}_p \nabla v, \nabla v)_\Omega + (\mu v, v)_{\Sigma_N} \\ &\geq \|\nabla v\|^2_{L^2(\Omega)} \\ &\geq \frac{1}{1 + C_P(\Omega)}\|v\|^2_{H^1(\Omega)}. \end{aligned}$$

For the second term,

$$\begin{aligned} a_\Lambda(V,V) &= \pi R^2 \left(k_w d_s V, d_s V\right) \geq \\ &\geq \pi R^2 k_{min} \|d_s V\|^2_{L^2(\Lambda)} \\ &\geq \pi R^2 k_{min} \frac{1}{1+C_p(\Lambda)} \|V\|^2_{H^1(\Lambda)}, \end{aligned}$$

where $C_p(\Lambda)$ denotes the constant in the stantard Poincaré inequality for $H^1_0(\Lambda)$ functions. As a result, the coercivity constant is

$$m = \min\left(\frac{1}{1+C_P(\Omega)}, \pi R^2 k_{min} \frac{1}{1+C_p(\Lambda)}\right).$$

In order to prove the continuity of the bilinear form $\mathcal{A}$ we consider again each term of $\mathcal{A}(u,v)$ separately. For the first bilinear form $a_\Omega(u,v)$ we have

$$\begin{aligned} a_\Omega(u,v) &= \left(\boldsymbol{k}_p \nabla u, \nabla v\right)_\Omega + \left(\mu u, v\right)_{\Sigma_N} \\ &\leq \max_{i,j} \|k_{p_{i,j}}\|_{L^\infty(\Omega)} \|\nabla u\|_{L^2(\Omega)} \|\nabla v\|_{L^2(\Omega)} + \|\mu\|_{L^\infty(\Sigma_N)} \|u\|_{L^2(\Sigma_N)} \|v\|_{L^2(\Sigma_N)} \\ &\leq \max_{i,j} \|k_{p_{i,j}}\|_{L^\infty(\Omega)} \|u\|_{H^1(\Omega)} \|v\|_{H^1(\Omega)} + C_T\left(\Sigma_N\right) \|\mu\|_{L^\infty(\Sigma_N)} \|u\|_{H^1(\Omega)} \|v\|_{H^1(\Omega)} \\ &\leq \left(\max_{i,j} \|k_{p_{i,j}}\|_{L^\infty(\Omega)} + C_T\left(\Sigma_N\right) \|\mu\|_{L^\infty(\Sigma_N)}\right) |||\mathcal{U}||| |||\mathcal{V}|||, \end{aligned}$$

where $C_T(\Sigma_N)$ is the constant of the trace inequality from $L^2(\Sigma_N)$ to $H^1(\Omega)$. For the second term $a_\Lambda(U,V)$, we easily obtain

$$a_\Lambda(U,V) = \pi R^2 \left(k_w d_s U, d_s V\right)_\Lambda \leq \pi R^2 \|k_w\|_{L^\infty(\Lambda)} \|U\|_{H^1(\Lambda)} \|V\|_{H^1(\Lambda)} \leq \pi R^2 \|k_w\|_{L^\infty(\Omega)} |||\mathcal{U}||| |||\mathcal{V}|||.$$

For the last term $b_\Lambda(\overline{u}-U, \overline{v}-V)$ using Lemma 1, we obtain

$$\begin{aligned} b_\Lambda(\overline{u}-U, \overline{v}-V) &\leq 2\pi R \|\kappa\|_{L^\infty(\Lambda)} \|\overline{u}-U\|_{L^2(\Lambda)} \|\overline{v}-V\|_{L^2(\Lambda)} \\ &\leq 2\pi R \|\kappa\|_{L^\infty(\Lambda)} \left(\|\overline{u}\|_{L^2(\Lambda)} + \|U\|_{L^2(\Lambda)}\right) \left(\|\overline{v}\|_{L^2(\Lambda)} + \|V\|_{L^2(\Lambda)}\right) \\ &\leq 2\pi R \|\kappa\|_{L^\infty(\Lambda)} \left(1 + \sqrt{\frac{C_T(\Gamma)}{2\pi R}}\right)^2 |||\mathcal{U}||| |||V|||. \end{aligned}$$

Therefore,

$$M = \max_{i,j} \|k_{p_{i,j}}\|_{L^\infty(\Omega)} + C_T\left(\Sigma_N\right) \|\mu\|_{L^\infty(\Sigma_N)} + \pi R^2 \|k_w\|_{L^\infty(\Omega)} + 2\pi R \|\kappa\|_{L^\infty(\Lambda)} \left(1 + \sqrt{\frac{C_T(\Gamma)}{2\pi R}}\right)^2.$$

Lemma 3 shows that the coercivity and continuity constants depend of the boundary conditions and the parameters of the problem. In particular, they are not robust with respect to R because $m \to 0$ in the limit $R \to 0$. In other words, the subproblem on Λ looses coercivity in the limit case.

Lemma 4 *The functional $\mathcal{F}$ is continuous in $\mathbb{V}$.*

Proof Indeed,

$$\mathcal{F}(\mathcal{V}) = -b_\Lambda(W,V) = -2\pi R \left(\kappa W, V\right)_\Lambda \leq 2\pi R \|\kappa\|_{L^\infty(\Lambda)} \|W\|_{L^2(\Lambda)} \|V\|_{L^2(\Lambda)} \leq 2\pi R \|\kappa\|_{L^\infty(\Lambda)} \|W\|_{L^2(\Lambda)} |||\mathcal{V}|||.$$

Theorem 1 *Problem* (10) *has a unique solution $\mathcal{U} \in \mathbb{V}$. Furthermore, the following stability estimate holds true,*

$$|||\mathcal{U}||| \leq \frac{1}{m} 2\pi R \|\kappa\|_{L^\infty(\Lambda)} \|W\|_{L^2(\Lambda)}. \tag{17}$$

Proof Owing to the Lax-Milgram Theorem, the result is a direct consequence of the previous lemmas.

3.1 Finite element approximation

Let us consider a quasi-uniform partition $\mathcal{T}_\Omega^h$ of Ω and an admissible partition $\mathcal{T}_\Lambda^h$ of Λ with the same characteristic size h and let $\mathbb{V}_h = V_h^\Omega \times V_h^\Lambda \subset \mathbb{V}$ be continuous k_1, k_2-order Lagrangian finite element space defined on $\mathcal{T}_\Omega^h$, $\mathcal{T}_\Lambda^h$ respectively. The numerical approximation of the variational formulation (10) consists of finding $\mathcal{U}_h \in \mathbb{V}_h$ solution of

$$\mathcal{A}(\mathcal{U}_h, \mathcal{V}_h) = \mathcal{F}(\mathcal{V}_h) \qquad \forall \mathcal{V}_h \in \mathbb{V}_h. \tag{18}$$

We notice that in problem (18) it is implicitly assumed that numerical integration is performed exactly. In practice, the average operator $\overline{(\cdot)}$ is approximated by means of numerical quadrature. The effect of this further approximation shall be analyzed in a future development of this work.

We exploit the conformity of the finite element space combined with Lemma 3, in order to prove that $\mathcal{U}_h$ satisfies a Ceá-type inequality,

$$|||\mathcal{U} - \mathcal{U}_h||| \leq \frac{M}{m} \inf_{v_h \in V_h^\Omega, V_h \in V_h^\Lambda} \left(\|u - v_h\|_{H^1(\Omega)} + \|U - V_h\|_{H^1(\Lambda)} \right). \tag{19}$$

The convergence of the finite element method follows from (19) combined with approximation properties of the finite element space. For the latter property, additional regularity of the solution is required. The solution U on Λ is in $H^2(\Lambda)$. The regularity of U descends from the standard theory of elliptic operators in convex domains, [10, Theorem 8.12], being W and $\overline{u}$ both in $L^2(\Lambda)$. Then, for the solution U on Λ, the standard finite element approximation estimate ensures that

$$\inf_{V_h \in V_h^\Lambda} \|U - V_h\|_{H^1(\Lambda)} \lesssim h^{r_2} \|U\|_{H^2(\Lambda)} \qquad r_2 = \min(k_2, 1),$$

where $a \lesssim b$ is equivalent to the inequality $a \leq Cb$ being C is a generic constant, possibly dependent on Ω but independent of the parameters of the problem.

Conversely, the regularity of u does not descends from standard results, because the right hand side in the first equation of (9) can be represented as a Dirac measure defined on Λ, the 1D manifold embedded into Ω. For this reason, we simply state the convergence result provided that u belongs to a suitable Sobolev space $W^{l,q}(\Omega)$. Let π^h be the Scott-Zhang interpolation operator from $W^{t,q}(\Omega) \cap H_0^1(\Omega)$ to V_h with $1 \leq q \leq \infty$ and $1 \leq t \leq l$ with the additional constraint $l > 1/q$ when $q > 1$. Then, the following interpolation estimate holds true (see for example [9] [Lemma 1.130])

$$\|v - \pi^h v\|_{W^{t,q}(\Omega)} \lesssim h^{r_1 - t} \|v\|_{W^{l,q}(\Omega)}, \quad r_1 = \min(l, k_1 + 1).$$

Therefore, combining (19) and the previous inequalities for piecewise affine approximation, we obtain

$$|||\mathcal{U} - \mathcal{U}_h||| \lesssim h^{r_1 - t} \|v\|_{W^{l,q}(\Omega)} + h^{r_2} \|U\|_{H^2(\Lambda)}.$$

4 Numerical solution strategies

In this section we analyze the properties of the matrix A arising from the discretization with linear finite elements of problem (10). We are particularly interested in investigating the performance of the Algebraic Multigrid Method (AMG) applied to this problem. For this purpose, we use the AMG library developed in [25,26,27].

Let us denote with $\varphi_{h,i}^* \in V_h^*$, $i = 1, \ldots, \dim(V_h^*)$ be the Lagrangian basis functions of V_h^*, where the symbol $*$ denotes either the domain Ω or Λ, and let $\boldsymbol{v}^* = \{v_i^*\}$ be the vector of the degrees of freedom relative to the generic finite element function v_h^* such that

$$v_h^* = \sum_{i=1}^{\dim(V_h^*)} v_i^* \varphi_{h,i}^*.$$

Let A be the stiffness matrix corresponding to the bilinear form $\mathcal{A}(\cdot, \cdot)$. More precisely, problem (10) is equivalent to the following algebraic problem,

$$A\boldsymbol{u} = \mathbf{f} \;\Leftrightarrow\; \begin{bmatrix} A^\Omega & -B \\ -B^T & A^\Lambda \end{bmatrix} \cdot \begin{bmatrix} \boldsymbol{u}^\Omega \\ \boldsymbol{u}^\Lambda \end{bmatrix} = \begin{bmatrix} \mathbf{0} \\ \mathbf{f}^\Lambda \end{bmatrix} \tag{20}$$

where the matrices and the right hand side have the following expressions

$$
\begin{aligned}
A^{\Omega}_{ij} &= \left(\boldsymbol{k}_p \nabla \varphi^{\Omega}_{h,j}, \nabla \varphi^{\Omega}_{h,i}\right) + \left(\mu \varphi^{\Omega}_{h,j}, \varphi^{\Omega}_{h,i}\right)_{\Sigma_N} + 2\pi R(\kappa \overline{\varphi}^{\Omega}_{h,j}, \overline{\varphi}^{\Omega}_{h,i})_{\Lambda}\,, \\
A^{\Lambda}_{ij} &= \pi R^2 (k_w d_s \varphi^{\Lambda}_{h,j}, d_s \varphi^{\Lambda}_{h,i})_{\Lambda} + 2\pi R(\kappa \varphi^{\Lambda}_{h,j}, \varphi^{\Lambda}_{h,i})_{\Lambda}\,, \\
B_{ij} &= 2\pi R(\kappa \varphi^{\Lambda}_{h,j}, \overline{\varphi}^{\Omega}_{h,i})_{\Lambda}\,, \\
\mathbf{f}^{\Lambda}_i &= -2\pi R(\kappa W, \varphi^{\Lambda}_{h,i})_{\Lambda}\,.
\end{aligned}
$$

We aim to study the system (20). We observe that, because of the different dimensionality, usually the discretization of Ω has many more degrees of freedom than the one of Λ. More precisely we have $\dim(V^{\Omega}_h) \gg \dim(V^{\Lambda}_h)$. Then, it is convenient to rewrite (20) as follows,

$$
\begin{aligned}
A^{\Lambda}\boldsymbol{u}^{\Lambda} &= \mathbf{f}^{\Lambda} + B^T \boldsymbol{u}^{\Omega}\,, \\
\left(A^{\Omega} - B\left(A^{\Lambda}\right)^{-1} B^T\right)\boldsymbol{u}^{\Omega} &= B\left(A^{\Lambda}\right)^{-1}\mathbf{f}^{\Lambda}\,.
\end{aligned}
$$

Since the matrix A^{Λ} can be easily solved and factorized because of the small size, this shows that the major cost for solving (20) is due to the subproblem on Ω. For this reason, in what follows we focus on the spectral properties and the solvers for matrix A^{Ω} solely. In this case, the discrete function identified by $\boldsymbol{u}^{\Lambda}$ is given a-priori. We name this problem as the *3D problem with 1D inclusions*.

4.1 Spectral properties and conditioning of the discrete 3D problem with 1D inclusions

We observe that A^{Ω} can be seen as the sum of a standard stiffness matrix (and possible boundary terms) with a matrix C^{Ω} relative to the coupling terms, such that $C^{\Omega}_{ij} = 2\pi R(\kappa\overline{\varphi}_{h,j}, \overline{\varphi}_{h,i})_{\Lambda}$. Since the coupling terms are non local, the sparsity pattern of the matrix will be significantly different than the one of a standard stiffness matrix. In this case, the rows of A^{Ω} may feature many non-zero entries. More precisely, Figure 2 shows the pattern of standard finite element stiffness matrix on the left, namely $\left(\boldsymbol{k}_p \nabla \varphi^{\Omega}_{h,j}, \nabla \varphi^{\Omega}_{h,i}\right)$, and on the right we show the new matrix modified by the 3D-1D coupling terms, namely matrix A^{Ω} defined above. We immediately observe that the coupling terms affect significantly the sparsity pattern of the algebraic problem. This poses some questions about the applicability of state of art numerical solvers to the problem, which will be directly addressed in the next section.

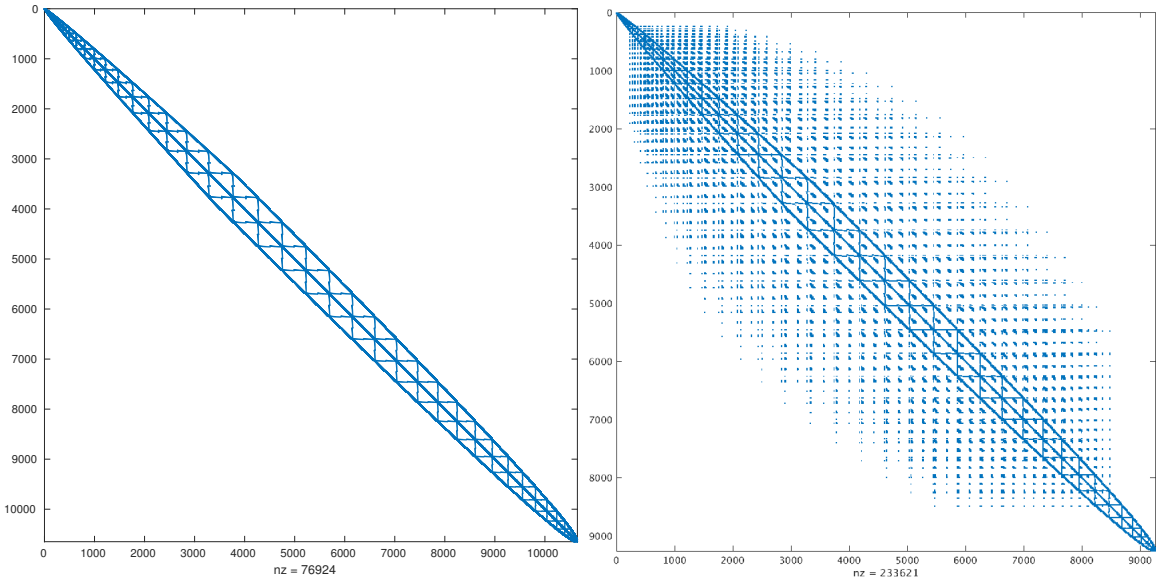

Fig. 2: The pattern of the standard stiffness matrix is reported on the left and compared with the pattern of the modified stiffness matrix A^{Ω}, on the right. The effect of the nonlocal coupling terms is clearly visible.

We proceed here with the analysis of the spectrum of A^Ω that is related to the bilinear form

$$A^\Omega_{ij} = \mathcal{A}^\Omega\left(\varphi^\Omega_{h,j}, \varphi^\Omega_{h,i}\right) = \left(\boldsymbol{k}_p \nabla\varphi^\Omega_{h,j}, \nabla\varphi^\Omega_{h,i}\right) + \left(\mu\varphi^\Omega_{h,j}, \varphi^\Omega_{h,i}\right)_{\Sigma_N} + 2\pi R(\kappa\overline{\varphi}^\Omega_{h,j}, \overline{\varphi}^\Omega_{h,i})_\Lambda.$$

The eigenvalues of a self-adjoint operator are real and for the largest and smallest eigenvalues the following expressions are valid:

$$\lambda_{min} = \min_{v^\Omega_h \neq 0 \in V^\Omega_h} \frac{\mathcal{A}^\Omega\left(v^\Omega_h, v^\Omega_h\right)}{\|\boldsymbol{v}^\Omega\|^2}, \qquad \lambda_{max} = \max_{v^\Omega_h \neq 0 \in V^\Omega_h} \frac{\mathcal{A}^\Omega\left(v^\Omega_h, v^\Omega_h\right)}{\|\boldsymbol{v}^\Omega\|^2},$$

where $\|\cdot\|$ is the standard Euclidean norm. In the case of Lagrangian finite elements in a three dimensional space, we have

$$h^3\|\boldsymbol{v}^\Omega\|^2 \lesssim \|v^\Omega_h\|^2_{L^2(\Omega)} \lesssim h^3\|\boldsymbol{v}^\Omega\|^2.$$

Using the continuity and the coercivity of $\mathcal{A}^\Omega$, we obtain

$$\lambda_{min} = \min_{v^\Omega_h \in V^\Omega_h} \frac{\mathcal{A}^\Omega(v^\Omega_h, v^\Omega_h)}{\|\boldsymbol{v}\|^2} \geq m^\Omega \frac{\|v^\Omega_h\|^2_{H^1(\Omega)}}{\|\boldsymbol{v}^\Omega\|} \geq m^\Omega \frac{\|v^\Omega_h\|^2_{L^2(\Omega)}}{\|\boldsymbol{v}^\Omega\|} \gtrsim m^\Omega h^3,$$

$$\lambda_{max} = \max_{v^\Omega_h \in V^\Omega_h} \frac{\mathcal{A}^\Omega\left(v^\Omega_h, v^\Omega_h\right)}{\|\boldsymbol{v}^\Omega\|^2} \lesssim M^\Omega \frac{\|v^\Omega_h\|^2_{H^1(\Omega)}}{\|\boldsymbol{v}^\Omega\|^2} \lesssim M^\Omega h^{-2} \frac{\|v^\Omega_h\|^2_{L^2(\Omega)}}{\|\boldsymbol{v}^\Omega\|^2} \lesssim M^\Omega h,$$

where, according to Lemma 3, constants m^Ω, M^Ω are the following,

$$m^\Omega = \frac{1}{1 + C_P(\Omega)}, \quad M^\Omega = \max_{i,j} \|k_{p_{i,j}}\|_{L^\infty(\Omega)} + C_T\left(\Sigma_N\right)\|\mu\|_{L^\infty(\Sigma_N)} + C_T(\Gamma)\|\kappa\|_{L^\infty(\Lambda)}.$$

For self-adjoint problems, upper and lower bounds of the spectrum give information about the spectral condition number $\mathcal{K}(\mathcal{A}^\Omega)$. Precisely, in this case we have

$$\mathcal{K}(\mathcal{A}^\Omega) \lesssim \frac{M^\Omega}{m^\Omega} h^{-2}.$$

From the previous spectral analysis, we deduce that the discretization in Ω is robust with respect to small inclusion radii, being the continuity and coercivity constants independent of R.

4.2 Application of Algebraic Multigrid to the solution of the 3D problem with 1D inclusions

The adequacy of the Algebraic Multigrid algorithm (AMG) to solve problems such as the one of Figure 2 (right) is an interesting question. On one hand, matrix A^Ω is symmetric positive definite, which makes AMG to be a good solution method. On the other hand, there are concerns about the influence of the modified sparsity patterns on the algebraic coarsening process. For example, Figure 3, shows how the sparsity pattern of matrix A^Ω changes after three levels of coarsening. The coarsest level (level three) is almost full and it is solved using a direct algorithm. Then, we aim to investigate how the coarsening algorithm transforms matrix A^Ω and how standard smoothing techniques behave when applied to these coarse problems. Finally, we will address the question of robustness of the solver with respect to reaction dominated problems with concentrated sources.

Keeping in mind the previous objectives, we review here some results about AMG. Since the recursive extension of any two level process to a multi-level process is formally straightforward, we describe the components of the AMG algorithm only on the basis of two level methods. Indices h and H mark the fine and the coarse level, respectively. We rewrite the sub-problem related to A^Ω as follows,

$$A^\Omega \boldsymbol{u}^\Omega = \boldsymbol{f}^\Omega \quad \Leftrightarrow \quad A_h \boldsymbol{u}_h = \boldsymbol{f}_h. \tag{21}$$

We remark that A_h in (21) stands for the matrix relative to the subproblem in Ω. It shall not be confused with the matrix of the coupled problem defined in (20). In this framework the coarse level system is

$$A_H \boldsymbol{u}_H = \boldsymbol{f}_H, \tag{22}$$

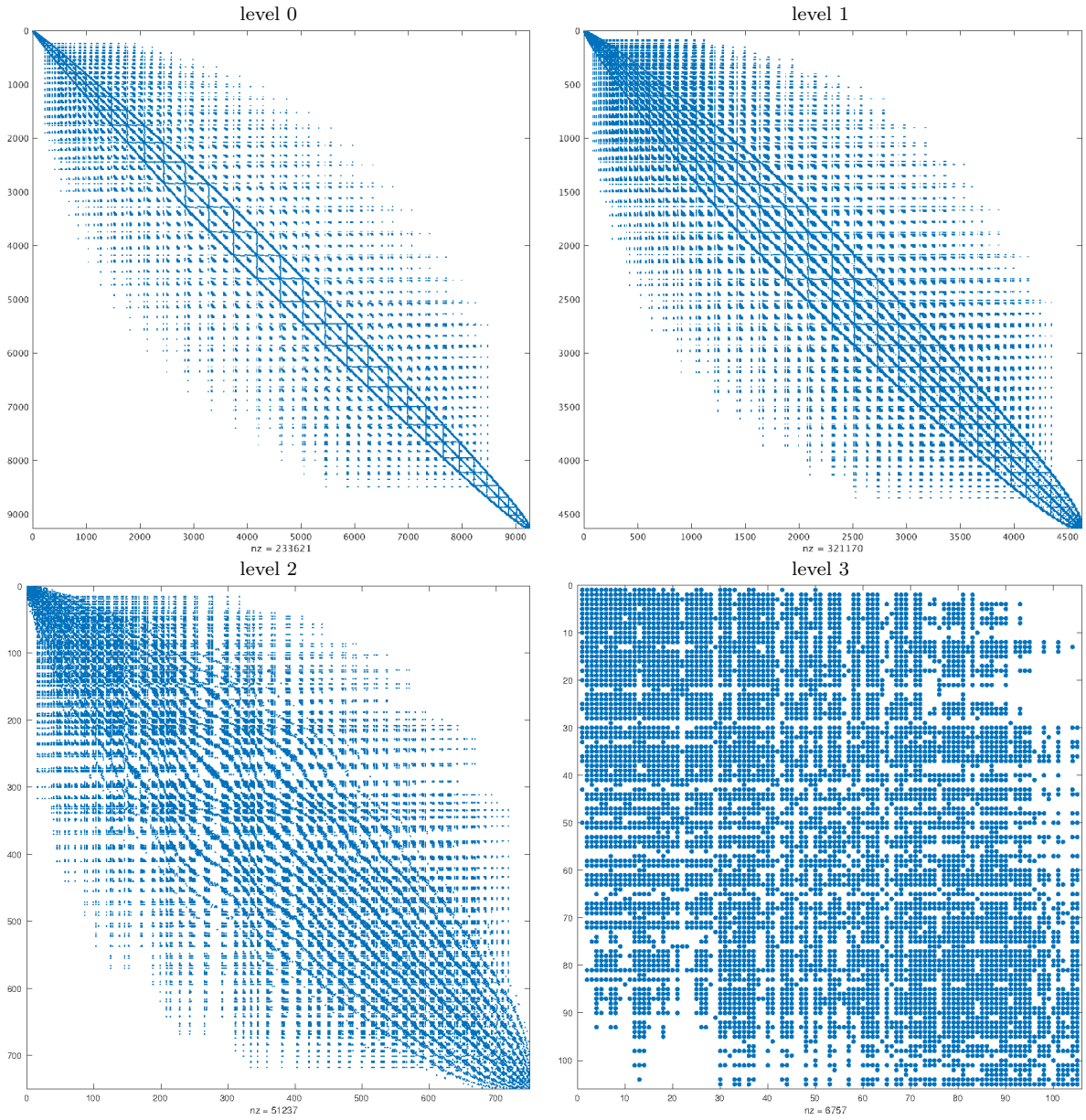

Fig. 3: Spartity patterns of the fine (level 0) and coarse levels (respectively 1, 2, 3) of the AMG solver.

where the matrix A_H is defined as the Galerkin operator

$$A_H := I_h^H A_h I_H^h \,, \tag{23}$$

where I_H^h and I_h^H denote the interpolation and the restriction operators, respectively.

We now define a smoothing process with a corresponding smoothing operator S_h as

$$\hat{\boldsymbol{u}}^h = S_h \boldsymbol{u}^h + (I_h - S_h) A_h^{-1} \boldsymbol{f}^h \,, \tag{24}$$

where I_h denotes the identity operator. We focus our attention on the Gauss-Seidel relaxation scheme, which implies the following choice of the smother

$$S_h = \left(I_h - Q_h^{-1} A_h\right) \,, \tag{25}$$

with Q_h being the lower triangular part of A_h.

We remark that A_h is a symmetric positive definite matrix for which we can define the restriction (I_h^H) as the transpose of interpolation (I_H^h). As a consequence A_H, defined in (23), is also symmetric and positive definite, *regardless* of the choice of I_H^h as long as it has full rank. In [26] the authors show that for a symmetric positive definite matrix any full rank interpolation operator generate a coarse level correction operator, which is an orthogonal projector with respect to the scalar product of $\mathcal{A}^\Omega$. In this case Galerkin based coarse grid corrections minimize the Euclidean norm of the error. Furthermore, the smoother iterations converge, because the operator S_h satisfies the *smoothing property*. More precisely, let $\boldsymbol{e}_h$ be the difference between the exact solution of (21) and the current approximation before smoothing. In [26] it is proven that for the smoother defined in (25), there exists σ, a strictly positive constant independent of $\boldsymbol{e}_h$, such that the following inequality holds true,

$$\|S_h \boldsymbol{e}_h\|_1^2 \leq \|\boldsymbol{e}_h\|_1^2 - \sigma \|\boldsymbol{e}_h\|_2^2 ,$$

where $\|\cdot\|_0$, $\|\cdot\|_1$ and $\|\cdot\|_2$ are norms induced by the following inner products,

$$(\boldsymbol{u},\boldsymbol{v})_0 = (D_h \boldsymbol{u},\boldsymbol{v}) , \quad (\boldsymbol{u},\boldsymbol{v})_1 = (A_h \boldsymbol{u},\boldsymbol{v}) , \quad (\boldsymbol{u},\boldsymbol{v})_2 = \left(D_h^{-1} A_h \boldsymbol{u}, A_h \boldsymbol{v}\right) , \quad D_h = diag(A_h).$$

This property implies that S_h is efficient in reducing the error $\boldsymbol{e}_h$ and more in general the performance of the AMG solver is good for symmetric positive definite problems such as (21). Moreover, the solver is not affected by the pattern of the matrix provided that the restriction operator has full rank and the coarsest problem can be appropriately handled (by a direct method).

We conclude this section with some considerations about the dependence of problem (10) form the physical parameters. In cases where $2\pi R\kappa \gg 1$, problem (10) is (locally) reaction dominated. As it will be discussed later, this is the case of applications to wells. The numerical experiments addressed in the next section suggest that the AMG solver is robust with respect to this case. This property can be justified following the lines of [24] and [20], where the convergence of the finite element method and of the geometric multigrid solver, respectively, are studied for reaction dominated problems.

The main reason why locally reaction-perturbed elliptic operators do not pose substantial problems at the level of finite element approximation, can be found in the analysis developed by Schatz and Wahlbin [24]. There, the authors prove the local uniform convergence of finite elements for singularly perturbed reaction-diffusion problems with Dirichlet boundary conditions, that is

$$\|u - u_h\|_{L^\infty(\Omega_0)} \leq C \ln^{\frac{3}{2}}(1/h) \min_{v_h \in V_h} \|u - v_h\|_{L^\infty(\Omega_1)} + C h^2 \ln^{\frac{1}{2}}(1/h), \tag{26}$$

where $\Omega_0 \subseteq \Omega_1 \subseteq \Omega$ and $\mathrm{dist}(\Omega_0, \partial\Omega_1) > 0$ and C denote generic constants uniformly independent of the parameters of the problem. This estimate confirms that uniform convergence takes place, away form the region where the singular behavior of the operator appears as a boundary layer. By exploiting this theory, Olshanskii and Reusken [20] have shown that the geometric multigrid method applied to reaction diffusion problems converges with a rate that is not affected by the physical parameters, because the deterioration of the approximation properties in the boundary layer are compensated by improved smoothing properties.

Even though we can not exhibit a rigorous proof, we observe that the uniform convergence rate of the multigrid method with respect to parameters applies also to our case, where reaction dominates the elliptic operator on some very local portions of the domain only. Again, this may be qualitatively justified by (26), because the effect to the singular perturbation does not affect the approximation away from the singularity.

5 Numerical experiments and discussion

In this section we support with numerical evidence the claims stated about the properties of the AMG solver applied to the *3D problem with 1D inclusions*. Afterward, we apply the *3D-1D coupled problem* to simulate some simple configurations of perforated reservoir.

5.1 Numerical experiments for the 3D problem with 1D inclusions

We consider a unit cubic domain $\Omega = (0,1)^3$ with a centered cylindrical inclusion of radius $R = \{0.01, 0.2\}$. The parameter κ is set equal to 1 and the source U varies linearly between 0 and 1. Homogeneous Neumann conditions are imposed on the boundary $\partial\Omega$. We use a family of four uniform meshes. A graphical description of the test case is shown in Figure 4.

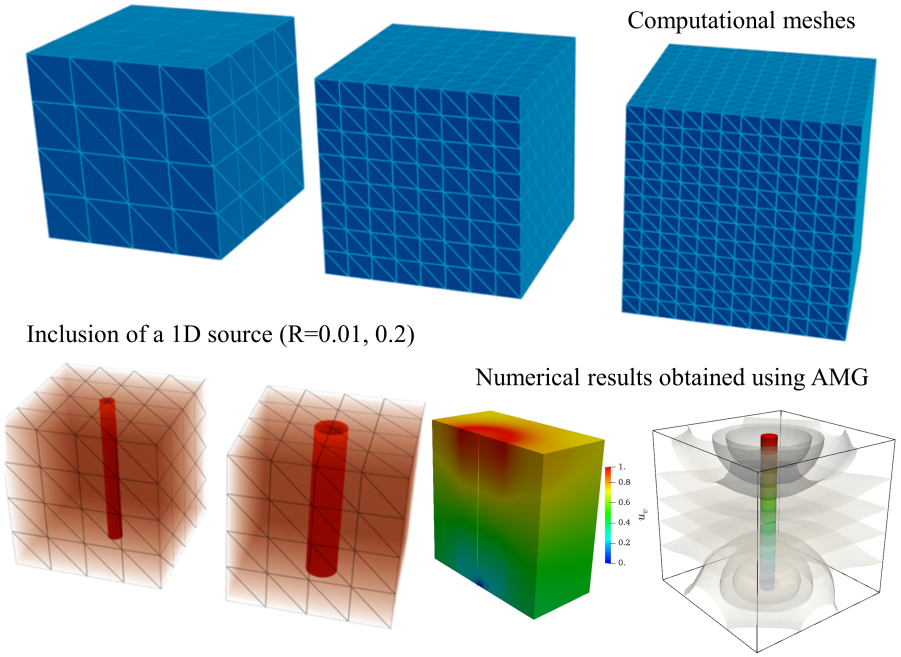

Fig. 4: Description of the 3D test case with 1D inclusions.

To solve the linear system deriving from the discrete formulation (18) we use the SAMG library, which provides both direct and AMG solvers for linear systems. We use the AMG solver on multiple V-cycle levels as a stand-alone solver (named stand-alone AMG), the AMG solver on multiple levels as a preconditioner for BiCGstab (accelerated AMG) and Intel's Pardiso as direct solver (also part of the library). Despite the name, there isn't any guarantee that the accelerated AMG outperforms the stand-alone approach. Indeed, for rather small matrices, the additional cost of initializing the data structures for the BiCGstab algorithm may offset the computational time of accelerated approach.

The results are reported in Table 1 and in Figure 5. We observe that in all the cases the numerical results confirm the theoretical expectations. More precisely, the computational cost scales with optimal complexity. Indeed, it is *linearly* dependent on the number of degrees of freedom (dof). On the contrary, as expected, the direct solver complexity is superlinear, in this case approximately *quadratic* with respect to the number of dof. This is a fundamental difference in performance, which makes the AMG solver 10 times faster than the direct solvers for systems with (only) 5×10^5 dof. We also observe that the solver is robust with respect to the main parameters of the problem, precisely R and κ, because the computational time is almost insensitive to variations of these.

Finally, the last dataset of Table 1 shows that the computational times for solving the standard stiffness matrix, namely $A^\Omega - C^\Omega$, or the modified matrix A^Ω are comparable (surprisingly less in the latter case). It means that the modified matrix pattern induced by the 3D-1D coupling terms does not affect the performance of AMG, even though it does modify the systems that are built and solved at the coarse levels. To sum up, the AMG solver is suitable for the problem at hand.

Test with $R = 0.01$, $\kappa = 1$.

Nb. of sub.	Nb. of dof	Nb. nz entries	Stand-alone AMG	Accelerated AMG	Pardiso
$[20, 20, 20]$	9261	7289	10,41299	10,62252	8,055254
$[40, 40, 40]$	68321	506289	16,61915	19,88221	18,01701
$[60, 60, 60]$	226981	1615081	25,33673	26,62287	123,8901
$[80, 80, 80]$	531441	3765281	44,91651	45,72543	680,3187

Test with $R = 0.2$, $\kappa = 1$.

Nb. of sub.	Nb. of dof	Nb. nz entries	Stand-alone AMG	Accelerated AMG	Pardiso
$[20, 20, 20]$	9261	253997	12,9794	11,07768	8,129677
$[40, 40, 40]$	68921	1483169	22,4713	24,79993	22,00561
$[60, 60, 60]$	226981	3298703	40,4724	38,28844	139,3998
$[80, 80, 80]$	531441	5785529	71,54043	67,63766	722,6398

Test with $R = 0.01$, $\kappa = 10$.

Nb. of sub.	Nb. of dof	Nb. nz entries	Stand-alone AMG	Accelerated AMG	Pardiso
$[20, 20, 20]$	9261	70837	10,71116	13,3264	8,448821
$[40, 40, 40]$	68921	1496781	16,13912	18,72223	21,52432
$[60, 60, 60]$	226981	1615081	24,45888	27,93736	117,4818
$[80, 80, 80]$	531441	3765281	47,71254	47,35248	694,8176

Test with $R = 0.01$, $\kappa = 100$.

Nb. of sub.	Nb. of dof	Nb. nz entries	Stand-alone AMG	Accelerated AMG	Pardiso
$[20, 20, 20]$	9261	69581	10,9014	14,10448	8,489918
$[40, 40, 40]$	68921	496013	13,93065	18,26737	20,187
$[60, 60, 60]$	22698	161508	25,92969	26,54227	116,3273
$[80, 80, 80]$	531441	3765281	45,92995	46,85656	658,9241

Test with $R = 0.01$, $\kappa = 1$, standard stiffness matrix $A - C$.

Nb. of sub.	Nb. of dof	Nb. nz entries	Stand-alone AMG	Accelerated AMG	Pardiso
$[20, 20, 20]$	9261	66981	10,78995	12,177191	8,389091
$[40, 40, 40]$	68921	491561	16,55888	17,38915	19,30781
$[60, 60, 60]$	22698	1609741	27,79404	28,93468	125,8552
$[80, 80, 80]$	531441	3757521	52,23508	50,62627	667,1364

Table 1: CPU time (seconds) for the solution of the linear system using SAMG library.

5.2 A 3D-1D coupled problem applied to reservoirs with two wells

We consider here data of a field experiment described in [16]. In particular, the computational domain is a slab located at the surface, of dimension $\Omega = L[0, 1] \times [0, 2/3] \times [-0.1, 0]$ where L=100 m. A sketch of the domain is shown in Figure 6. In dimensionless coordinates, the wells are located at $x = 1/3$, $y = 1/3$ (labelled with B in Figure 6) and in $x = 2/3$, $y = 1/3$ (labelled with A) and they extend to the entire thickness of the domain.

We assume that the material that surrounds the wells is isotropic. As a result, for a given value of K_p the tensor $\boldsymbol{k}_p$ is the identity in problem (3). The wells are much more permeable to flow than the reservoir. For this reason, we take $k_w = 1000$ in dimensionless form. Finally, we assume that the permeability of the well surface is larger than the intrinsic one of the rock. More precisely, we assume that it scales as $K = 100K_p/\rho$ that implies $\kappa = 100L/\rho = 100/R$.

We address *two test cases*, that differ for the boundary conditions enforced at the endpoints of the wells, while on the external boundary $\partial\Omega$ homogeneous Neumann conditions are imposed. In the first one (named *Test 1*), we assume that the injection well (A) is subject to an overpressure equal to the atmospheric one. At depth $z = -L_2 = -0.1$ (points A_2 and B_2) we enforce a pressure equal to $0.7p_{w,0}$ and at the top of the production well is open to the atmosphere. The overview of the numerical solution in both the slab and the wells is shown in Figure 7. The Darcy velocity in the slab is visualized by the arrows. Also the injection and the extraction wells are marked in the same way. The pressure field is visualized by means of the color scale in Figure 7. In particular, Figure 7 shows the pressure field together with the isobaric curve in the middle plane of the domain ($z = -0.05$). From these results we conclude that all the expected behaviors of the problem are captured by the proposed scheme. More precisely, the

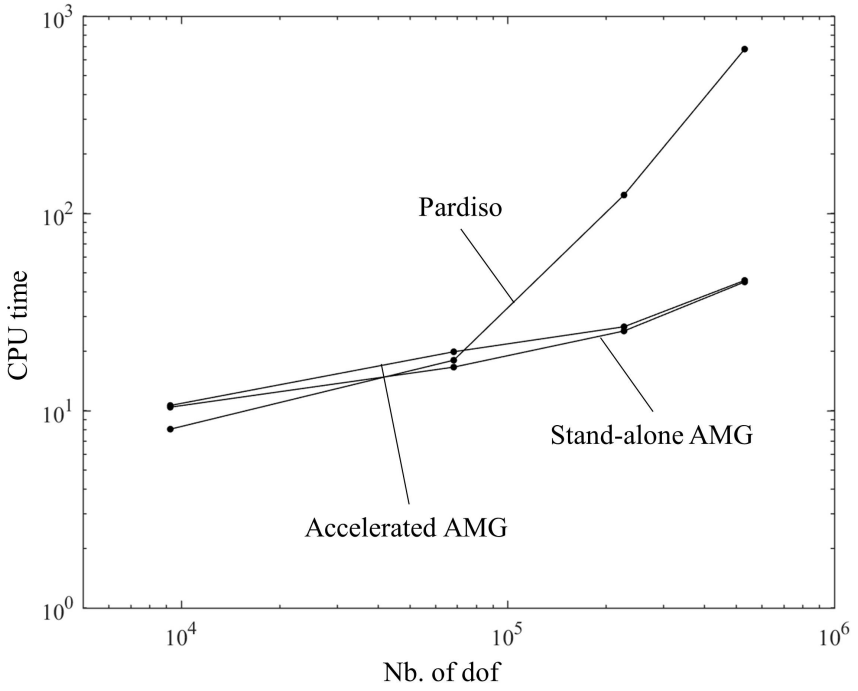

Fig. 5: CPU time (seconds) for the solution of the linear sistem using SAMG library.

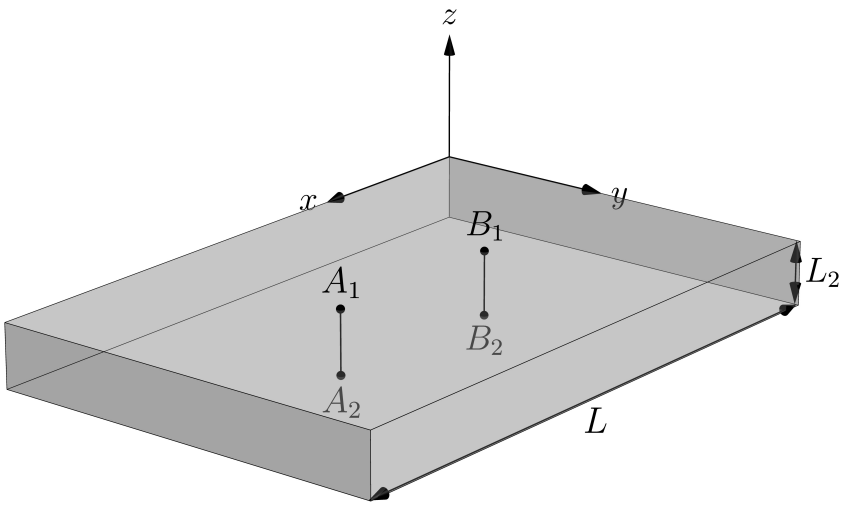

Fig. 6: Geometrical description of the problem.

injected fluid travels towards the extraction well and a moderate pressure gradient is established inside the slab. Finally, in Figure 8 we plot the dimensionless pressure in the wells. We notice that the pressure varies linearly along the wells, matching the prescribed values at the endpoints. As a result, the velocity is almost constant and each well carries an almost steady flow. Only a small part of it leaks-off to the exterior from the lateral surface of the wells.

In the other test case (named *Test 2*), the bottom end of the wells is impermeable to flow. More precisely, an injection pressure equal to $p_{w,0}$ is set at the surface (point A_1), while no-flux condition is enforced at depth $z = -L_2 = -0.1$ (point A_2). For the production well we assume that the surface endpoint is exposed to the atmospheric pressure (point B_1) while no-flux condition is set at depth $z = -L_2 = -0.1$ (point B_2). As shown in Figure 8, pressure is almost constant along each well. This setting resembles the case with prescribed sources analyzed in section 3.

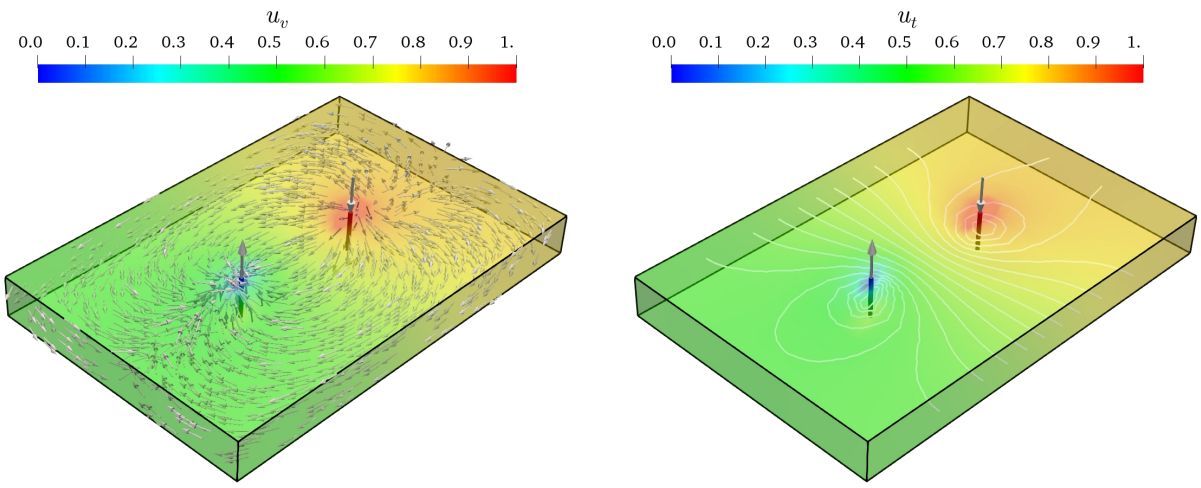

Fig. 7: Test 1: (Left panel) Pressure field in the 3D/1D domain, the vectors point in the direction of the flow. (Right panel) Pressure field in the 3D/1D domain together with the isoline of the pressure field in the middle plane ($z = -0.05$).

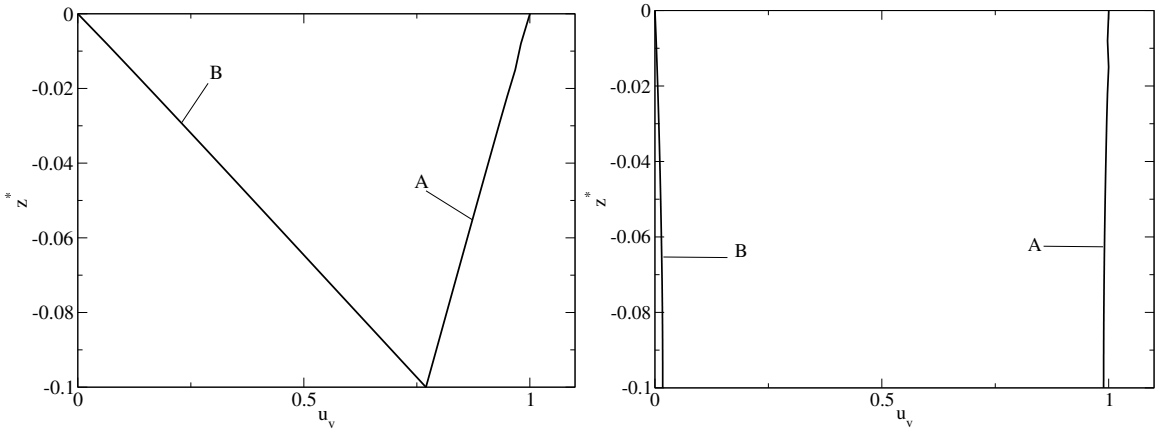

Fig. 8: Pressure field in the injection (A) and the extraction (B) well, left panel is Test 1 and right panel is Test 2, respectively.

The maps of flow and pressure of *Test 2* are reported in Figure 9. Comparing these results with the ones of the previous test, we observe that the pressure gradient in this case is more marked than before. It means that more flow propagates through the slab. This can be explained noticing that the wells are closed at the bottom. As a result, all the fluid that enters the injection well at the top must reach the extraction well.

5.3 A 3D-1D coupled problem applied to reservoirs with multiple wells

Here we test the ability of the model and of the corresponding implementation to handle multiple wells. In particular, thanks to the generality of the formulation, which does not require any conformity between the computational meshes and the discretization of the 3D and 1D subdomains, handling several wells does not poses any additional difficulty than modeling only two of them.

In Figure 10, we show the simulations obtained with two idealized configurations. All the parameters and boundary conditions are the same than the ones of Test 1. On the top we have multiple production wells located on the surface of a cone with axis aligned with the injection well. This configuration forms a sort of pressure cushion around the production well. On the bottom, we have randomly located the

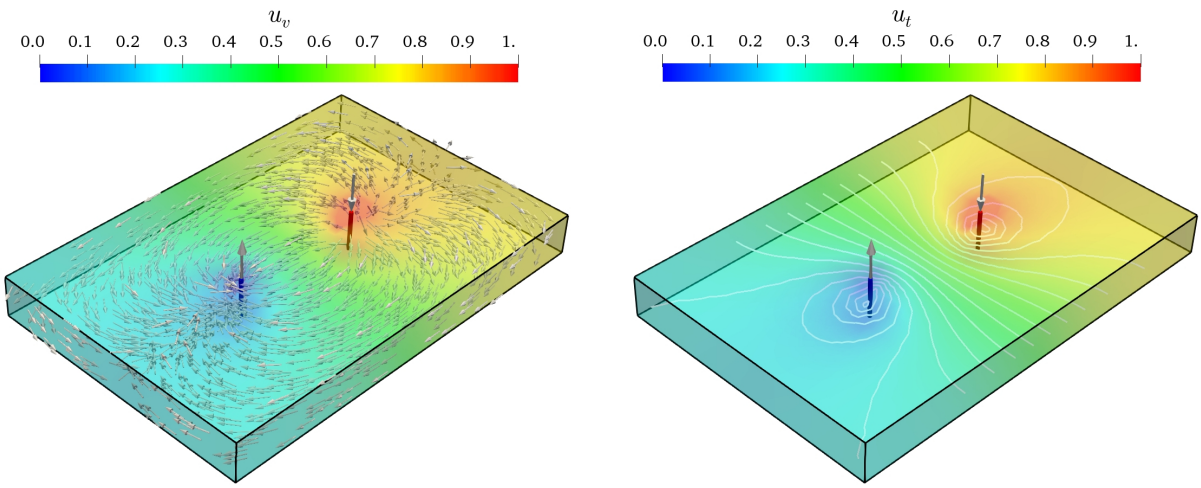

Fig. 9: Test 2: (Left panel) Pressure field in the 3D/1D domain, the vectors point in the direction of the flow. (Right panel) Pressure field in the 3D/1D domain tohether with the isoline of the pressure field in the middle plane.

endpoints of the wells on the top and bottom surfaces of the slab. We notice that the pressure field reflects the pattern of the wells while the velocity is rather chaotic.

6 Conclusions

We have developed a computational approach to model the interaction of wells with a reservoir. The problem shows non-standard features: (i) at the level of modeling for the application of topological model reduction techniques; (ii) at the level of analysis because it consists of coupled PDEs defined on manifolds of different dimensionality; and (iii) at the level of numerical discretization because it corresponds to a linear system with an unusual pattern.

A natural development of this work, already in progress, consists of extending the model and the analysis to the mixed formulation of the flow, where both pressure and velocity fields are modeled and approximated simultaneously. A preliminary report of this study is available in [19]. More in general, this approach can be extended to model fractures, fracture tips and wells as two-dimensional (2D) and one-dimensional (1D) manifolds embedded into a three-dimensional (3D) reservoir. We believe that this extension would be particularly attractive for subsurface flow applications, because it provides a unified approach to model the fluid injection and borehole interaction with the surrounding reservoir (using the 3D-1D multiscale coupling) and the formation of the fracture network (using the 3D-2D-1D approach for the interaction of reservoir, fracture and fracture tip, respectively).

Acknowledgements The author names are listed in alphabetical order. All the authors are members of the INdAM Research group GNCS. The author Federica Laurino acknowledges the support of the Italian Institute of Technology with the fellowship: *Sviluppo di metodi computazionali di tipo multi-scala per la simulazione del trasporto vascolare ed extra vascolare di molecole, nano-costrutti e cellule in tessuti neoplastici.*

References

1. Bellout, M., Echeverra Ciaurri, D., Durlofsky, L., Foss, B., Kleppe, J.: Joint optimization of oil well placement and controls. Computational Geosciences **16**(4), 1061–1079 (2012). DOI 10.1007/s10596-012-9303-5
2. Boon, W., Nordbotten, J., Vatne, J.: Mixed-dimensional elliptic partial differential equations. Tech. rep., arXiv, Cornell University Library (2017). ArXiv:1710.00556v2
3. Cattaneo, L., Zunino, P.: A computational model of drug delivery through microcirculation to compare different tumor treatments. International Journal for Numerical Methods in Biomedical Engineering **30**(11), 1347–1371 (2014). DOI 10.1002/cnm.2661
4. Cattaneo, L., Zunino, P.: Computational models for fluid exchange between microcirculation and tissue interstitium. Networks and Heterogeneous Media **9**(1), 135–159 (2014). DOI 10.3934/nhm.2014.9.135

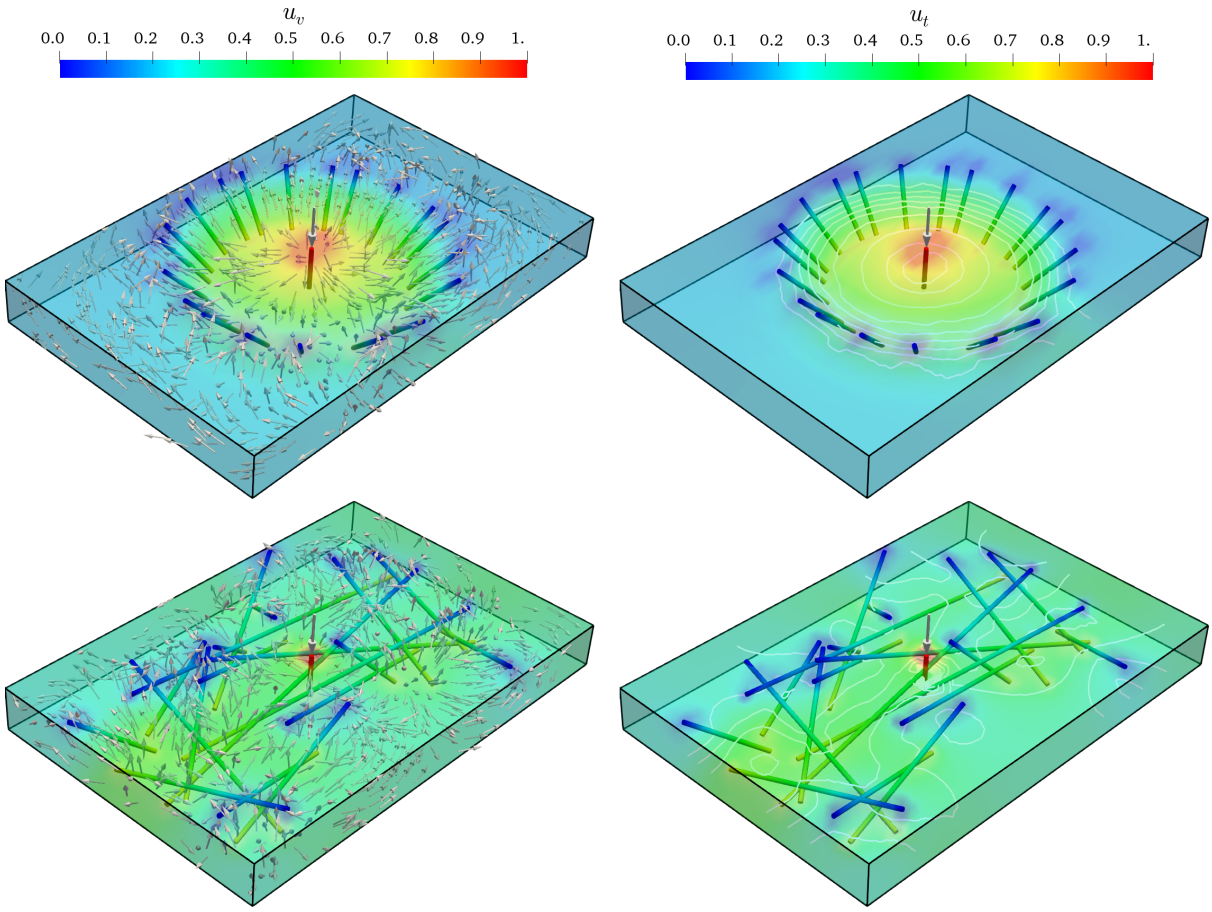

Fig. 10: Pressure (with isoline of the pressure field in the middle plane at $z = -0.05$) and velocity vector fields (arrows denote the dicection, not the magnitude) in the 3D/1D domain, for two idealized configurations with multiple wells. Parameters and boundary conditions are the same of Test 1.

5. Chen, Z., Yue, X.: Numerical homogenization of well singularities in the flow transport through heterogeneous porous media. Multiscale Modeling and Simulation **1**(2), 260–303 (2003). DOI 10.1137/S1540345902413322
6. D'Angelo, C.: Multi scale modelling of metabolism and transport phenomena in living tissues, PhD Thesis. EPFL, Lausanne (2007)
7. D'Angelo, C.: Finite element approximation of elliptic problems with dirac measure terms in weighted spaces: Applications to one- and three-dimensional coupled problems. SIAM Journal on Numerical Analysis **50**(1), 194–215 (2012). DOI 10.1137/100813853
8. D'Angelo, C., Quarteroni, A.: On the coupling of 1d and 3d diffusion-reaction equations. application to tissue perfusion problems. Mathematical Models and Methods in Applied Sciences **18**(8), 1481–1504 (2008). DOI 10.1142/S0218202508003108
9. Ern, A., Guermond, J.L.: Theory and practice of finite elements, *Applied Mathematical Sciences*, vol. 159. Springer-Verlag, New York (2004). DOI 10.1007/978-1-4757-4355-5
10. Gilbarg, D., Trudinger, N.: Elliptic Partial Differential Equations of Second Order, vol. 224. Springer Science & Business Media (2001)
11. Jenny, P., Lunati, I.: Modeling complex wells with the multi-scale finite-volume method. Journal of Computational Physics **228**(3), 687–702 (2009). DOI 10.1016/j.jcp.2008.09.026
12. Koeppl, T., Vidotto, E., Wohlmuth, B., Zunino, P.: Mathematical modelling, analysis and numerical approximation of second order elliptic problems with inclusions. Mathematical Models and Methods in Applied Sciences **28**(05) (2018)
13. Köppl, T., Vidotto, E., Wohlmuth, B.: A local error estimate for the poisson equation with a line source term. In: Numerical Mathematics and Advanced Applications ENUMATH 2015, pp. 421–429. Springer (2016)
14. Köppl, T., Wohlmuth, B.: Optimal a priori error estimates for an elliptic problem with dirac right-hand side. SIAM Journal on Numerical Analysis **52**(4), 1753–1769 (2014)
15. Kuchta, M., Nordaas, M., Verschaeve, J., Mortensen, M., Mardal, K.A.: Preconditioners for saddle point systems with trace constraints coupling 2d and 1d domains. SIAM Journal on Scientific Computing **38**(6), B962–B987 (2016). DOI 10.1137/15M1052822
16. Lee, K.S.: Efficiency of horizontal and vertical well patterns on the performance of micellar-polymer flooding. Energy Procedia **16**, 889–894 (2012)
17. Nabil, M., Decuzzi, P., Zunino, P.: Modelling mass and heat transfer in nano-based cancer hyperthermia. Royal Society Open Science **2**(10) (2015). DOI 10.1098/rsos.150447

18. Nabil, M., Zunino, P.: A computational study of cancer hyperthermia based on vascular magnetic nanoconstructs. Royal Society Open Science **3**(9) (2016). DOI 10.1098/rsos.160287
19. Notaro, D., Cattaneo, L., Formaggia, L., Scotti, A., Zunino, P.: A Mixed Finite Element Method for Modeling the Fluid Exchange Between Microcirculation and Tissue Interstitium, pp. 3–25. Springer International Publishing (2016). DOI 10.1007/978-3-319-41246-7-1
20. Olshanskii, M., Reusken, A.: On the convergence of a multigrid method for linear reaction-diffusion problems. Computing (Vienna/New York) **65**(3), 193–202 (2000)
21. Peaceman, D.: Interpretation of well-block pressures in numerical reservoir simulation. Soc Pet Eng AIME J **18**(3), 183–194 (1978)
22. Peaceman, D.: Interpretation of well-block pressures in numerical reservoir simulation - part 3: Some additional well geometries. pp. 457–471 (1987)
23. Peaceman, D.W.: Interpretation of well-block pressures in numerical reservoir simulation with nonsquare grid blocks and anisotropic permeability. Society of Petroleum Engineers journal **23**(3), 531–543 (1983). DOI 10.2118/10528-PA
24. Schatz, A.H., Wahlbin, L.B.: On the finite element method for singularly perturbed reaction-diffusion problems in two and one dimensions. Math. Comp. **40**(161), 47–89 (1983)
25. Stüben, K.: Algebraic multigrid (amg): experiences and comparisons. Applied Mathematics and Computation **13**(3-4), 419–451 (1983). DOI 10.1016/0096-3003(83)90023-1
26. Stüben, K.: Algebraic Multigrid (AMG): An Introduction with Applications; Updated Version of GMD Report No 53, March 1999. GMD-Report. GMD-Forschungszentrum Informationstechnik (1999)
27. Stüben, K., Clees, T., Klie, H., Lu, B., Wheeler, M.: Algebraic multigrid methods (amg) for the efficient solution of fully implicit formulations in reservoir simulation. pp. 59–69 (2007)
28. Wolfsteiner, C., Lee, S., Tchelepi, H.: Well modeling in the multiscale finite volume method for subsurface flow simulation. Multiscale Modeling and Simulation **5**(3), 900–917 (2006). DOI 10.1137/050640771
29. Wu, Y.S.: A virtual node method for handling well bore boundary conditions in modeling multiphase flow in porous and fractured media. Water Resources Research **36**(3), 807–814 (2000). DOI 10.1029/1999WR900336

MOX Technical Reports, last issues

Dipartimento di Matematica
Politecnico di Milano, Via Bonardi 9 - 20133 Milano (Italy)

53/2018 Giantesio, G.; Musesti, A.; Riccobelli, D.
A comparison between active strain and active stress in transversely isotropic hyperelastic materials

54/2018 Dal Santo, N.; Deparis, S.; Manzoni, A.; Quarteroni, A.
Multi space reduced basis preconditioners for parametrized Stokes equations

52/2018 Possenti, L.; di Gregorio, S.; Gerosa, F.M.; Raimondi, G.; Casagrande, G.; Costantino, M.L.; Z
A computational model for microcirculation including Fahraeus-Lindqvist effect, plasma skimming and fluid exchange with the tissue interstitium

51/2018 Stella, S.; Vergara, C.; Giovannacci, L.; Quarteroni, A.; Prouse, G.
Assessing the disturbed flow and the transition to turbulence in the arteriovenous fistula

50/2018 Gervasio, P.; Quarteroni, A.
The INTERNODES method for non-conforming discretizations of PDEs

49/2018 Massi, M.C.; Ieva, F.; Lettieri, E.
Data Mining Application to Healthcare Fraud Detection: A Two-Step Unsupervised Clustering Model for Outlier Detection with Administrative Databases

48/2018 Arnone, E.; Azzimonti, L.; Nobile, F.; Sangalli, L.M.
Modeling spatially dependent functional data via regression with di fferential regularization

47/2018 Stefanucci, M.; Sangalli, L.M.; Brutti, P.
PCA-based discrimination of partially observed functional data, with an application to Aneurisk65 dataset

46/2018 Riccobelli, D.; Ciarletta, P.
Morpho-elastic model of the tortuous tumour vessels

45/2018 Bernardi, M.S.; Carey, M.; Ramsay, J.O.; Sangalli, L.M.
Modeling spatial anisotropy via regression with partial di fferential regularization